

Amplified melt and flow of the Greenland ice sheet driven by late-summer cyclonic rainfall

Samuel H. Doyle^{1*}, Alun Hubbard², Roderik S. W. van de Wal³, Jason E. Box^{4,5}, Dirk van As⁴, Kilian Scharrer⁶, Toby W. Meierbachtol⁷, Paul C. J. P. Smeets³, Joel T. Harper⁷, Emma Johansson^{8,9}, Ruth H. Mottram¹⁰, Andreas B. Mikkelsen¹¹, Frank Wilhelms^{12,13}, Henry Patton², Poul Christoffersen¹⁴ and Bryn Hubbard¹

Intense rainfall events significantly affect Alpine and Alaskan glaciers through enhanced melting, ice-flow acceleration and subglacial sediment erosion, yet their impact on the Greenland ice sheet has not been assessed. Here we present measurements of ice velocity, subglacial water pressure and meteorological variables from the western margin of the Greenland ice sheet during a week of warm, wet cyclonic weather in late August and early September 2011. We find that extreme surface runoff from melt and rainfall led to a widespread acceleration in ice flow that extended 140 km into the ice-sheet interior. We suggest that the late-season timing was critical in promoting rapid runoff across an extensive bare ice surface that overwhelmed a subglacial hydrological system in transition to a less-efficient winter mode. Reanalysis data reveal that similar cyclonic weather conditions prevailed across southern and western Greenland during this time, and we observe a corresponding ice-flow response at all land- and marine-terminating glaciers in these regions for which data are available. Given that the advection of warm, moist air masses and rainfall over Greenland is expected to become more frequent in the coming decades, our findings portend a previously unforeseen vulnerability of the Greenland ice sheet to climate change.

The Greenland ice sheet (GIS) is the largest cryospheric contributor to global sea-level rise: responsible for 0.7 mm yr⁻¹—a rate at least double that of the Antarctic ice sheets combined and one that has steadily accelerated over the past two decades^{1,2}. Approximately half of this mass loss is attributed to summer, surface melt processes enhanced through a number of positive feedbacks, such as surface albedo and hypsometry, which are relatively well constrained and amenable to modelling under future climate change^{1,3}. The remaining dynamic mass losses are attributed to increased ice discharge and are clearly significant yet remain poorly constrained and difficult to model and predict². Here we present evidence for a large, late-summer, cyclonically induced runoff event that falls outside the surface melt processes included in mass-loss assessments, and which had a potent and widespread effect on surface melt and ice dynamics.

In this study, we test the hypothesis that late-season cyclonic weather systems—which are predicted to increase in frequency and magnitude^{4,5} yet have so far been neglected in studies of GIS dynamics and mass balance^{1,2}—produce sufficient runoff to overwhelm the ice sheet's basal drainage system, driving transient, widespread accelerations in ice flow. We focus our investigation on the Kangerlussuaq sector of the GIS where a dense network

of Global Positioning System (GPS) receivers and automated weather stations (AWS), plus borehole water-pressure and proglacial discharge records, enable a comprehensive analysis of the meteorological and glaciological conditions driving a late-summer acceleration event in 2011. We then use reanalysis data to determine the synoptic weather and spatial footprint of this specific event, before interrogating meteorological, regional climate modelling and ice surface velocity records from around Greenland to determine the magnitude, impact and frequency of this and other similar events in the past. This analysis provides a framework for the reinterpretation of three well-documented ice-flow acceleration events that were previously attributed to surface melt alone. Finally, we discuss the implications of these findings in the context of predicted changes in Greenland's climate over the next century.

Runoff and ice dynamics in the Kangerlussuaq sector

Seasonal and inter-annual acceleration of GIS flow is governed by the dynamic response of the basal hydrologic system to variability in meltwater delivery to the bed^{6–14}. The highest ice velocities typically occur shortly after melt onset, when an inefficient drainage system is overwhelmed by the first major inputs of surface water of the melt

¹Centre for Glaciology, Department of Geography & Earth Sciences, Aberystwyth University, Aberystwyth SY23 3DB, UK. ²Centre for Arctic Gas Hydrate, Environment and Climate, Department of Geology, The Arctic University of Norway, N-9037 Tromsø, Norway. ³Institute for Marine and Atmospheric Research Utrecht, Utrecht University, PO Box 80005, 3508TA Utrecht, Netherlands. ⁴Geological Survey of Denmark and Greenland, Øster Voldgade 10, 1350 Copenhagen K, Denmark. ⁵Department of Geography, The Ohio State University, 1036 Derby Hall, 154 North Oval Mall, Columbus, Ohio 43210-1361, USA. ⁶ENVEO IT GmbH, Innsbruck 6020, Austria. ⁷Department of Geosciences, University of Montana, Missoula, Montana 59812, USA. ⁸Department of Physical Geography and Quaternary Geology, Bert Bolin Centre for Climate Research, Stockholm University, SE-106 91 Stockholm, Sweden. ⁹Swedish Nuclear Fuel and Waste Management Co, Box 250, SE-101 24 Stockholm, Sweden. ¹⁰Danish Meteorological Institute, Lyngbyvej 100, DK-2100 Copenhagen Ø, Denmark. ¹¹Department of Geosciences and Natural Resource Management, University of Copenhagen, Øster Voldgade 10, DK-1350 Copenhagen, Denmark. ¹²Alfred-Wegener-Institut Helmholtz-Zentrum für Polar- und Meeresforschung, Am Handelshafen 12, 27570 Bremerhaven, Germany. ¹³Department of Crystallography, Geoscience Centre, University of Göttingen, Goldschmidtstraße 1, 37077 Göttingen, Germany. ¹⁴Scott Polar Research Institute, University of Cambridge, Lensfield Road, Cambridge CB2 1ER, UK. *e-mail: sdd08@aber.ac.uk

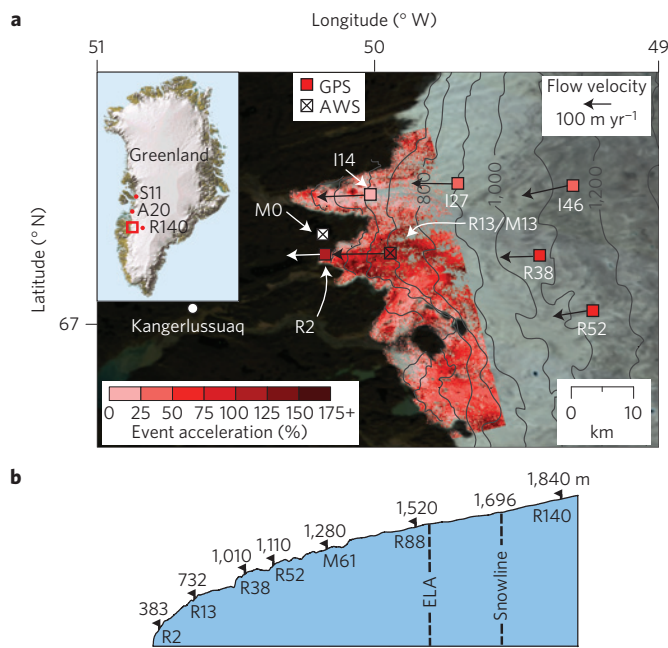


Figure 1 | The study area. a, Map of the lower ablation area of the Kangerlussuaq sector. The background MODIS image was acquired on 17 August 2011. Acceleration during the late-August event (23 August–3 September 2011) relative to the preceding period (1–23 August 2011) was derived from TanDEM-X velocity maps. The GPS symbol colours represent the percentage of acceleration during the event (Supplementary Table 1). The velocity vector shows the mean velocity during the late-August acceleration. The red square in the inset map shows the location in Greenland. **b**, Russell Glacier's elevation profile with the ELA and snowline marked.

season, with the lowest velocities usually observed in late summer and autumn when declining melt inputs are easily accommodated by an efficient and well-developed basal hydrologic system^{7–11}.

The seasonal velocity cycles recorded at nine GPS sites on Russell Glacier and Isunngata Sermia in West Greenland during 2011 (Fig. 1) are consistent with these systematic variations with one exception: a prominent flow acceleration between 24 August and 1 September (Fig. 2d,e). Surface velocities derived from offset tracking with TanDEM-X data show widespread acceleration of up to 220% across a large portion of the ice-sheet margin for the interval 23 August–3 September compared with the preceding period (1–23 August; Fig. 1 and Supplementary Fig. 1). During the event, velocities at Russell Glacier GPS sites R2, R13, R38, R52 and R88 (where the number denotes kilometres from the glacier's terminus) increased by 117, 140, 71, 64 and 46% above those of the preceding week (Supplementary Table 1). The acceleration was particularly large at site R13 (Fig. 2d) where the daily mean velocity of 365 m yr⁻¹ during the event exceeded the site's melt onset peak of 337 m yr⁻¹ on 8 June, which typically represents the highest velocity within any given year^{7,8,11}. The pronounced flow response was present across all neighbouring glaciers, including Isunngata Sermia, which accelerated by 22%, 58% and 55% at I14, I27 and I46 respectively (Figs 1 and 2d and Supplementary Table 1), and was also detectable—albeit muted—140 km into the ice-sheet interior, well within the accumulation zone at R140 (Fig. 2e).

We ascribe this flow acceleration to an intense period of surface runoff composed of both rainfall and melt. Measured rainfall during the event accounted for 20% (23.6 mm) of the annual total (115.1 mm) and despite such rainfall being uncommon for the Kangerlussuaq region¹⁵, surface melt was the primary contributor to runoff. Furthermore, although the highest melt rates during the

event (for example, 3.2 mm water equivalent (w.e.) h⁻¹ at M13 on 27 August, Fig. 3b) were less than peak summer values (for example, 6 mm w.e. h⁻¹ at M13 on 30 July 2011), they were unusually sustained throughout both day and night by enhanced long-wave radiation and turbulent heat fluxes^{16,17} associated with the advection of warm, moist air into the region (Figs 3 and 4 and Supplementary Fig. 2; see Meteorological measurements in Methods). This unusually sustained period of continuous melt totalled 331 mm w.e. at M13 between 24 August and 1 September, representing 10% of the annual total and twice that of the preceding week (Fig. 3b). Given the upper estimate of rainfall of 24 mm, ice surface melt accounted for at least 93% of the overall runoff at M13 (732 m above sea level; asl) during the event. Measured melt was only slightly lower at higher elevations: at M61 (1,280 m asl) 315 mm w.e. of melt during the event accounted for a disproportionate percentage (15%) of the annual total (Fig. 2b). Melting extended throughout the entire ablation area, and beyond the mean (1990–2011) equilibrium line altitude¹⁸ (ELA) of 1,553 m asl. Although rain-induced ice melt was minimal at M13 (1.1–1.8 mm w.e.), the heat released by rain freezing into the surface snowpack enhanced melt above the snowline (1,696 m asl). For instance, 14 mm of rain at 2 °C freezing in the snowpack would bring 15 cm w.e. of snow at –15 °C to the melting point (see Meteorological measurements in Methods). At site M140 (1,840 m asl), situated well above the snowline, 50 mm w.e. of melt (8% of the annual total) was recorded between 24–29 August, concurrent with above-freezing air temperatures (Supplementary Fig. 2). Virtually all precipitation occurred during this period and precipitation estimates (13–23 mm) suggest that at higher elevations rainfall contributed a larger proportion (for example, 18–32% at M140) to the runoff than at lower elevations. The highest daily precipitation totals on 27 August (8.4 mm in Kangerlussuaq and 3.9 mm at M0) were coincident with the highest daily total melt (for example, 53 mm w.e. at M13), and a transient excursion of the freezing level from ~1,000 m asl to 2,450 m asl, which is ~900 m above the long-term ELA (Supplementary Fig. 2c).

Owing to the ice sheet's hypsometry, the surface area that receives precipitation as rain and is exposed to melt increases nonlinearly with a rising freezing level (Fig. 1b). We attribute the extremely high freezing level on 27 August (Supplementary Fig. 2), which indicates that melt and rainfall occurred up to 280 km inland, to the advection of warm, moist air over the GIS from the southwest (Fig. 4). As a saturated air mass rises its cooling rate decreases owing to the latent heat released by condensation. Accordingly, the lapse rate during the event was significantly lower (0.48 °C 100 m⁻¹) than the annual mean (0.70 °C 100 m⁻¹) and condensation at the ice surface resulted in an increased—and abnormally positive—latent heat flux that contributed 18% to the energy available for melting on 27 August (Fig. 3a). Melting consequently extended well into the accumulation area and across almost a third of the entire GIS on this day¹⁹.

Crucially, the event occurred in late summer when buffering of surface runoff in snowpack and firn was at an annual minimum. The decadal-high, end-of-season snowline (1,696 m asl) exposed a large expanse of bare ice (Fig. 1b), and runoff during the event would have been efficiently concentrated into a mature network of channels and moulins developed during the preceding summer months, thereby facilitating rapid discharge into the subglacial environment. Nevertheless, total runoff during the late-August event was lower than mid-summer values when ice velocities were below the annual mean, implying that runoff volume is not the only factor governing the acceleration we observe (Fig. 2). The seasonal evolution of subglacial drainage from an inefficient/distributed to an efficient system explains low mid-summer ice velocities at times of high melt input^{7–12}, and previous studies^{20,21} suggest that the antecedent subglacial conditions modulate basal sliding. It is therefore significant that the event reported here occurred in late summer, immediately following a period of sub-zero air

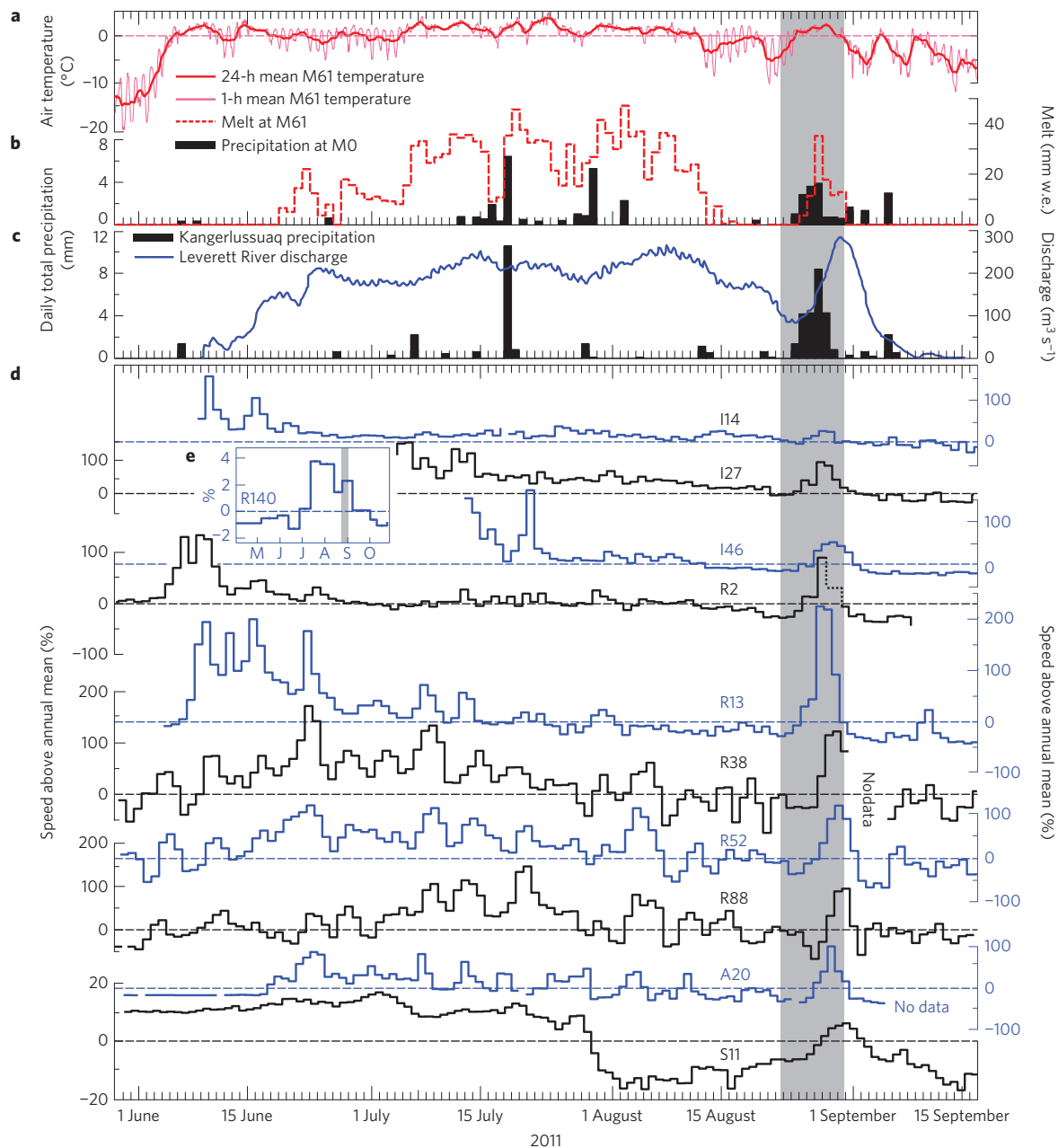


Figure 2 | Records of meteorology, proglacial discharge, and ice velocity for the 2011 melt season. a, Air temperature at M61 with a 1- and 24-h average applied. **b,** Daily total melt at M61 and precipitation at M0. **c,** Precipitation in Kangerlussuaq and proglacial Leverett River discharge¹³. **d,e,** Daily averaged velocity at 11 GPS sites on land-terminating Russell Glacier (R) and Isunngata Sermia (I) and marine-terminating Store Glacier³⁰ (S) and Sermeq Avannarleq⁶ (A), expressed as speed above the annual mean. Note the different y-axis scaling for S11 and R140. The timing of the late-August acceleration is shaded in grey.

temperatures (Fig. 2a) and rapidly declining meltwater production: no melt was recorded at M61 for the week before the event (Fig. 2b). On 21 August, temperatures at the lowest-elevation AWS, M13, dropped below freezing for the first time since melt onset on 1 June resulting in the lowest daily melt rates, proglacial discharge and ice velocities since that date (Figs 2 and 3). We interpret the gradual reduction in diurnal variability and simultaneous increase in borehole water pressure at R13 during the preceding period (Fig. 3) as evidence of a pre-event transition of the basal hydrologic system to a less efficient winter-type mode^{6,12}. The 3-day-lagged peak in proglacial discharge (Fig. 2c), of unprecedented magnitude in 2011 and which represents 13% of the annual total, supports this hypothesis as water transit is retarded under inefficient subglacial

drainage conditions²². Hence, the late-summer timing of the event critically dictated the ice sheet's dynamic response: the preceding week of sub-zero air temperatures (Fig. 2a) and declining melt (Figs 2 and 3) primed the ice sheet for a high-magnitude flow response to this late-August runoff perturbation.

The rapid increases in subglacial water pressure recorded in two boreholes on Russell Glacier (at R13), as well as those measured on Isunngata Sermia²³ and Sermeq Avannarleq⁶, to levels exceeding the ice overburden pressure suggest that the ice sheet was hydraulically decoupled from its bed during the acceleration event (Fig. 3c). This is confirmed by decimetre-scale surface uplift recorded at R13 (Fig. 3c) and at site A20 on Sermeq Avannarleq⁶. Uplift was sustained at R13 for ~22 h before the surface lowered,

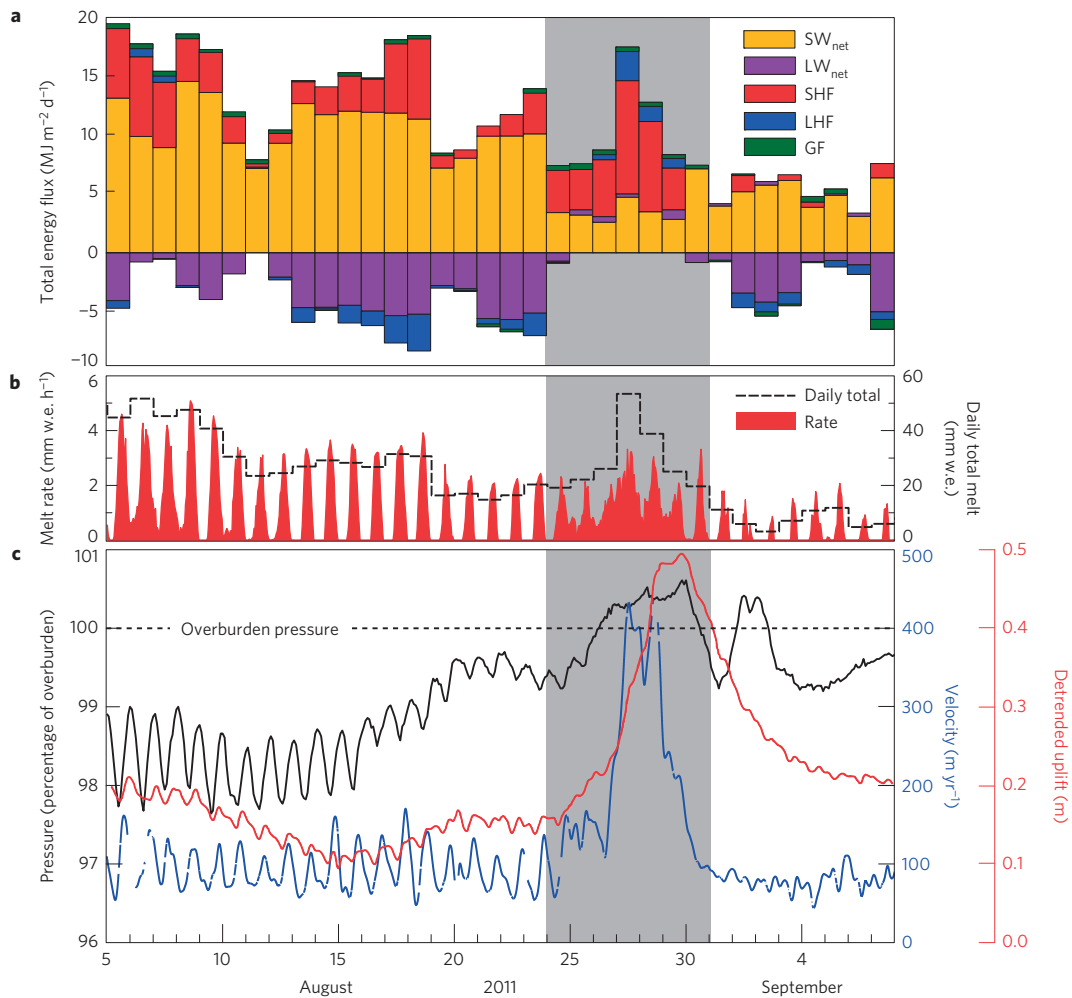


Figure 3 | The surface energy budget, melt, borehole water pressure and ice surface velocity and uplift at R13. **a**, The surface energy budget at M13 at a daily time step. The components: net short-wave (SW_{net}) and net long-wave (LW_{net}) radiation, the sensible (SHF) and latent (LHF) heat fluxes and the ground flux (GF) are defined as positive when they add heat to the surface. **b**, Surface melt rate and total daily melt. **c**, Borehole water pressure, ice surface velocity and ice surface uplift. The timing of the late-August acceleration is shaded in grey.

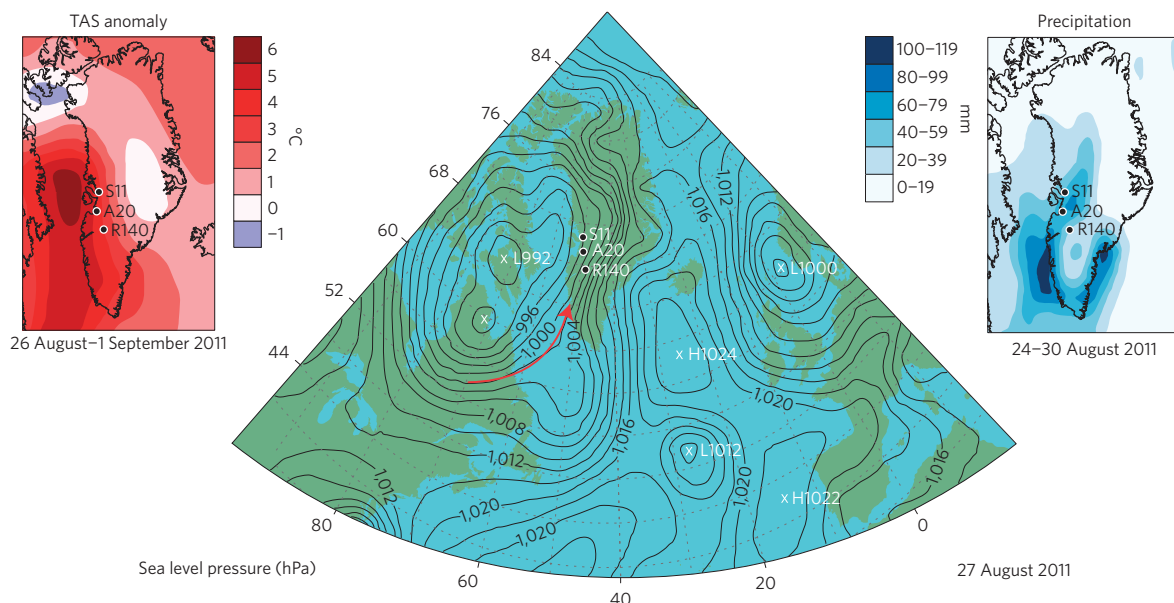


Figure 4 | Reanalysis data for the August/September 2011 event including sea-level pressure for 27 August 2011, the near-surface air temperature (TAS) anomaly for the period 26 August–1 September versus the same period in the 1981–2010 baseline, and total precipitation for the week 26–30 August. The red arrow indicates the direction of warm air advection. Data from ref. 27.

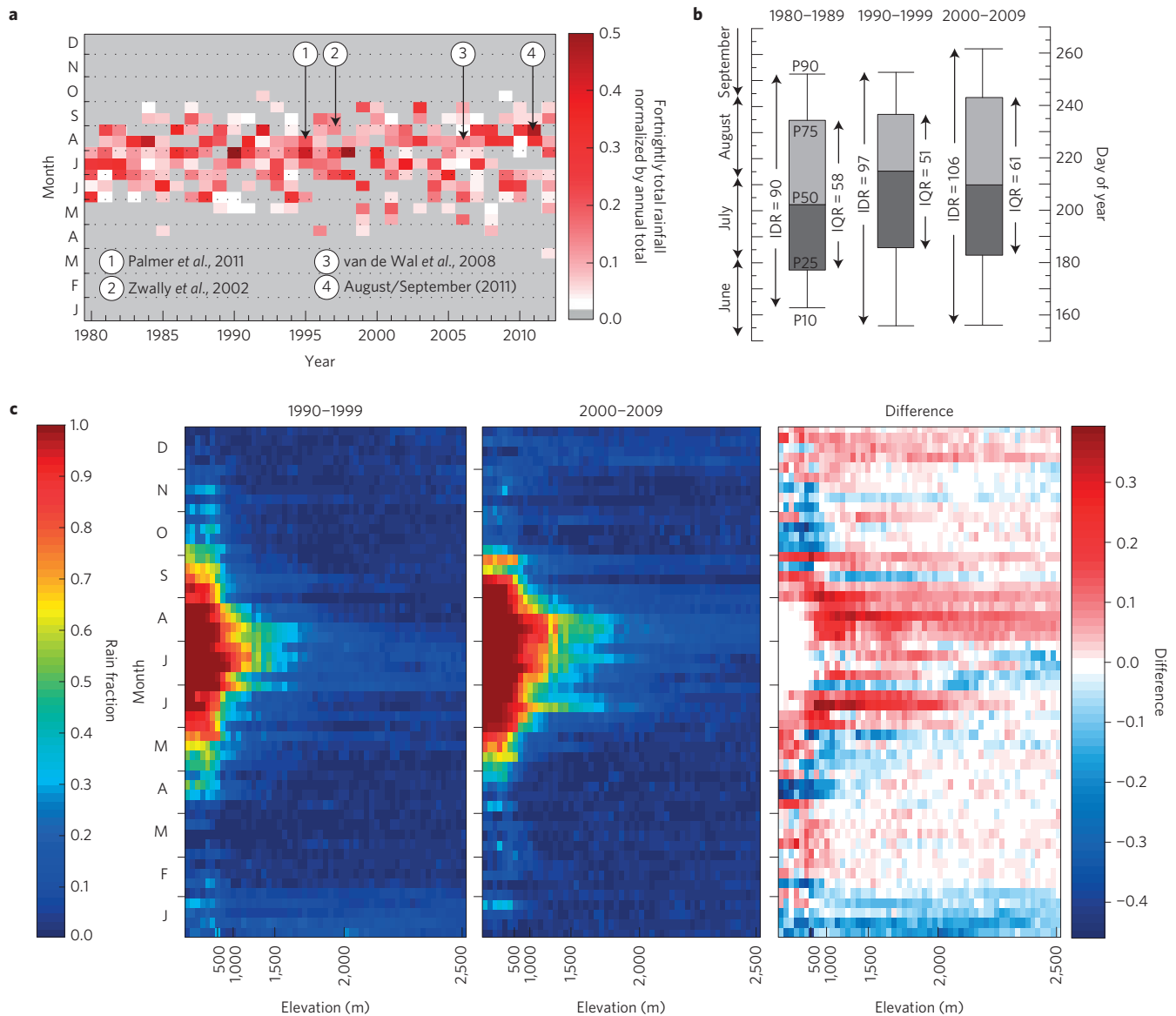


Figure 5 | Long-term trends in rainfall seasonality and elevation. **a**, Fortnightly total rainfall in Kangerlussuaq normalized by the annual total between 1980 and 2012. Arrows indicate the 2011 event and three events evident in recent studies^{14,33,34}. **b**, The decadal mean day of year on which the percentiles in total annual rainfall in Kangerlussuaq were achieved. **c**, HIRHAM5 regional climate model simulations of the rain fraction across the K-transect at a weekly time step. Heavy rainfall events appear on **a** as dark red blocks. The interquartile (IQR) and interdecile (IDR) ranges with units of days are annotated on **b**.

returning to its pre-event height by 12:30 UTC on 3 September (Fig. 3c). Consistent with the theory of cavity opening²⁴, peak flow acceleration was coincident with the highest rates of water pressure and uplift change, not their maxima. The sudden drops in water pressure and ice velocity on 31 August to levels lower than those before the acceleration event suggest that the rapid post-event decline in surface runoff delivered a markedly reduced water flux to a drainage system with temporary overcapacity^{12,21}.

It is worth noting that rainfall events occurring earlier in the summer (for example, 10 mm in Kangerlussuaq on 18 July) had no pronounced dynamic response (Fig. 2) as they did not challenge the capacity of what can be interpreted as an efficient subglacial drainage system at this time⁷⁻¹². Importantly, the glaciological and meteorological conditions inherent to the late-August event preferentially occur in late summer when the drainage system is closing down and cannot efficiently drain high runoff volumes. The advection of cyclonic weather systems over the GIS is most frequent in August²⁵, and accordingly August is the wettest¹⁵ and cloudiest²⁶

month in this region, with the heaviest rainfall (Fig. 5a) and peak net long-wave radiation²⁶.

The spatial extent and frequency of these events

The acceleration event in late August 2011 provides a unique natural experiment to investigate the dynamic response of the GIS to a spatially extensive and well-defined runoff perturbation. For eight days during late August and early September 2011, reanalysis data²⁷ indicate that a cyclone (minimum surface pressure of 992 hPa) centred on Baffin Bay off the west coast of Greenland advected warm, southwesterly airflow over the GIS, bringing extensive precipitation, which was especially heavy in southeast Greenland (Fig. 4 and Supplementary Fig. 9). These observations are consistent with lee cyclogenesis whereby an Icelandic low-pressure system forms in the lee of the GIS off the southeast coast, while the parent cyclone delivers precipitation to west Greenland as it tracks north up the Davis Strait^{28,29}. Occurring on 3.5% of all days between 1961-1999, and 6.3% of days in summer, Baffin Bay cyclones

represent the most frequent synoptic pattern to deliver precipitation to Greenland²⁹. Reanalysis data confirm that the weather conditions driving the late-August acceleration prevailed across southern and western Greenland (Fig. 4).

We find that a concomitant flow response is evident in all available velocity records from these regions, including three major marine-terminating glaciers located up to 370 km north of Kangerlussuaq: ice flow increased by 9% and 95% above the preceding week at GPS sites on Store Glacier³⁰ (S11) and Sermeq Avannarleq⁶ (A20) respectively (Fig. 2d and Supplementary Table 1). Repeat InSAR data³¹ reveal that ice flow also increased by 10% on Jakobshavn Isbræ between 23 August and 3 September 2011 compared with 2–13 August (Supplementary Fig. 3). The lower relative increase in ice velocity for the lower tongues of Store Glacier and Jakobshavn Isbræ (that is, up to 10–15 km from the calving front) is not unexpected because it is well established that the termini of fast marine-terminating glaciers experience smaller relative increases in velocity in response to surface water inputs compared with interior and land-terminating regions of the ice sheet that are remote from tidewater influences³². Simultaneous ice acceleration at all sites with contemporaneous data indicates that runoff during the late-August 2011 event overwhelmed the basal hydrologic system of at least eight glaciers in southern and western Greenland (Figs 1 and 2), including both land- and marine-terminating outlets. The acceleration in ice flow extended at least 140 km into the ice-sheet interior (Fig. 2e), and we infer that this flow response was not just restricted to those sectors of the ice sheet with available velocity measurements.

Moreover, three previous late-summer acceleration and uplift events identified on the GIS in recent studies^{14,33,34} can, with hindsight, now be reinterpreted as cyclonic rainfall/melt events (Fig. 5a). Previously, these pronounced acceleration events were interpreted as characteristic of late-summer melt-induced acceleration^{14,33,34}, which given their timing does not conform with the typical seasonal velocity cycle identified by subsequent studies^{7–11}. Reanalysis data and meteorological records (Supplementary Figs 4–7 and 10–12 and Supplementary Section 1) reveal that these events were all driven by cyclonic conditions similar to those during late August 2011. Many additional late-summer rainfall events are apparent from analysis of precipitation records (Fig. 5a), although, unfortunately, velocity data are not available to determine the specific flow response to each of these perturbations.

Future impact on ice-sheet mass balance and dynamics

Our findings lead us to the question of whether annual ice flow will increase in the future given predictions of a warmer, wetter climate. The delivery of surface water to the bed accelerates ice flow over the course of summer¹⁴ yet recent studies^{13,34–36} suggest that annual ice flow in the ablation area is regulated by the melt-induced seasonal transition from inefficient/distributed to efficient subglacial drainage. Our observations support the hypothesis that high-magnitude inputs of water to the bed have the capacity to reorganize the basal drainage system, resulting in lower velocities following the event than preceded it^{20,21,37}. It follows that, by establishing efficient subglacial drainage, such events will yield reduced post-event velocities and could therefore regulate ice flow over annual timescales^{13,34–36,38}. Although this self-regulation model seems to hold across the ablation area¹³ and on Alaskan glaciers³⁸, where melt inputs to the basal drainage system are high and thin ice results in low basal conduit closure rates, this generalized model is unlikely to hold under a succession of late-season, cyclonic perturbations as described herein. Nor will flow within the interior of the GIS self-regulate as thicker ice, lower net surface melt rates and shallower surface and bed slopes hinder the development of efficient subglacial drainage and its regulating influence^{23,39,40}. Multi-year observations of increasing ice flow within the accumulation area of the GIS

(ref. 41) provide support for this premise. Furthermore, higher-order three-dimensional ice-flow modelling⁴² indicates that the net annual flow and discharge of the GIS is indeed sensitive to and will increase in response to a greater frequency and spatial extent of high-magnitude runoff events anticipated under a warmer climate.

The advection of warm, moist air masses and rainfall over Greenland is predicted to become more frequent through the twenty-first century, in response to a warmer and cloudier regional climate and a northward shift in storm tracks^{4,5,43–45}. Consistent with modelling experiments⁴³, analysis of Kangerlussuaq precipitation records and HIRHAM5 model simulations reveal that the seasonal distribution of rainfall has already increased over the past thirty years, with a tendency for a higher proportion of rain falling later in the season (Fig. 5 and Supplementary Fig. 8) when the subglacial drainage system is likely to be highly sensitive to water inputs. A larger fraction of precipitation already falls as rain across the GIS (ref. 46), and rain now falls at higher elevations (Fig. 5c) where the ice sheet is responsive to increased runoff⁴¹. Cyclonic-induced runoff events may therefore play a more prominent role in the mass balance and dynamics of the GIS than they have previously, and their importance will increase if predicted changes in Greenland's climate^{4,5,43–45,47} are realized.

Methods

Methods and any associated references are available in the [online version of the paper](#).

Received 13 April 2015; accepted 10 June 2015;
published online 13 July 2015

References

- Hanna, E. *et al.* Ice-sheet mass balance and climate change. *Nature* **498**, 51–59 (2013).
- Vaughan, D. G. *et al.* in *Climate Change 2013: The Physical Science Basis* (eds Stocker, T. F. *et al.*) Ch. 4 (IPCC, Cambridge Univ. Press, 2013).
- van den Broeke, M. *et al.* Partitioning recent Greenland mass loss. *Science* **326**, 984–986 (2009).
- Schuenemann, K. C. & Cassano, J. J. Changes in synoptic weather patterns and Greenland precipitation in the 20th and 21st centuries: 2. Analysis of 21st century atmospheric changes using self-organizing maps. *J. Geophys. Res.* **115**, D05108 (2010).
- Vavrus, S. J. Extreme Arctic cyclones in CMIP5 historical simulations. *Geophys. Res. Lett.* **40**, 6208–6212 (2013).
- Andrews, L. C. *et al.* Direct observations of evolving subglacial drainage beneath the Greenland Ice Sheet. *Nature* **514**, 80–83 (2014).
- Bartholomew, I. *et al.* Seasonal evolution of subglacial drainage and acceleration in a Greenland outlet glacier. *Nature Geosci.* **3**, 408–411 (2010).
- Bartholomew, I. *et al.* Seasonal variations in Greenland Ice Sheet motion: Inland extent and behaviour at higher elevations. *Earth Planet. Sci. Lett.* **307**, 271–278 (2011).
- Bartholomew, I. *et al.* Short-term variability in Greenland Ice Sheet motion forced by time-varying meltwater drainage: Implications for the relationship between subglacial drainage system behavior and ice velocity. *J. Geophys. Res.* **117**, F03002 (2012).
- Colgan, W. *et al.* The annual glaciology cycle in the ablation zone of the Greenland ice sheet: Part 1. Hydrology model. *J. Glaciol.* **57**, 697–709 (2011).
- Hoffman, M. J., Catania, G. A., Neumann, T. A., Andrews, L. C. & Rumrill, J. A. Links between acceleration, melting, and supraglacial lake drainage of the western Greenland Ice Sheet. *J. Geophys. Res.* **116**, F04035 (2011).
- Schoof, C. Ice-sheet acceleration driven by melt water supply variability. *Nature* **468**, 803–806 (2010).
- Sole, A. *et al.* Winter motion mediates dynamic response of the Greenland Ice Sheet to warmer summers. *Geophys. Res. Lett.* **40**, 3940–3944 (2013).
- Zwalf, J. H. *et al.* Surface melt-induced acceleration of Greenland ice-sheet flow. *Science* **297**, 218–222 (2002).
- Cappelen, J., Jørgensen, B. V., Laursen, E. V., Stannius, L. S. & Thomsen, R. S. *The Observed Climate of Greenland, 1958–99—with Climatological Standard Normals, 1961–90* Technical Report 00-18 (Danish Meteorological Institute, 2001); http://www.dmi.dk/fileadmin/user_upload/Rapporter/TR/2000/tr00-18.pdf

16. Gascon, G., Sharp, M. & Bush, A. Changes in melt season characteristics on Devon Ice Cap, Canada, and their association with the Arctic atmospheric circulation. *Ann. Glaciol.* **54**, 101–110 (2013).
17. van den Broeke, M. R., Smeets, C. J. J. P. & van de Wal, R. S. W. The seasonal cycle and interannual variability of surface energy balance and melt in the ablation zone of the west Greenland ice sheet. *Cryosphere* **5**, 377–390 (2011).
18. van de Wal, R. S. W. *et al.* Twenty-one years of mass balance observations along the K-transect, West Greenland. *Earth Syst. Sci. Data* **4**, 31–35 (2012).
19. Mernild, S. H. & Liston, G. E. Surface melt extent for the Greenland Ice Sheet, 2011. *Geogr. Tidsskr.* **112**, 84–88 (2012).
20. Fudge, T. J., Harper, J. T., Humphrey, N. F. & Pfeffer, W. T. Rapid glacier sliding, reverse ice motion and subglacial water pressure during an autumn rainstorm. *J. Glaciol.* **50**, 101–107 (2009).
21. O'Neel, S., Echelmeyer, K. A. & Motyka, R. J. Short-term flow dynamics of a retreating tidewater glacier: LeConte Glacier, Alaska U.S.A. *J. Glaciol.* **47**, 567–578 (2001).
22. Chandler, D. M. *et al.* Evolution of the subglacial drainage system beneath the Greenland Ice Sheet revealed by tracers. *Nature Geosci.* **6**, 195–198 (2013).
23. Meierbachtol, T., Harper, J. & Humphrey, N. Basal drainage system response to increasing surface melt on the Greenland ice sheet. *Science* **341**, 777–779 (2013).
24. Iken, A. The effect of the subglacial water pressure on the sliding velocity of a glacier in an idealized numerical model. *J. Glaciol.* **27**, 407–421 (1981).
25. Serreze, M., Box, J., Barry, R. & Walsh, J. Characteristics of Arctic synoptic activity, 1952–1989. *Meteorol. Atmos. Phys.* **51**, 147–164 (1993).
26. van den Broeke, M., Smeets, P., Ettema, J. & Munneke, P. K. Surface radiation balance in the ablation zone of the west Greenland ice sheet. *J. Geophys. Res.* **113**, D13105 (2008).
27. Kalnay, E. *et al.* The NCEP/NCAR 40-year reanalysis project. *Bull. Am. Meteorol. Soc.* **77**, 437–471 (1996).
28. Chen, Q.-s., Bromwich, D. H. & Bai, L. Precipitation over Greenland retrieved by a dynamic method and its relation to cyclonic activity. *J. Clim.* **10**, 839–870 (1997).
29. Schuenemann, K. C., Cassano, J. J. & Finniss, J. Synoptic forcing of precipitation over Greenland: Climatology for 1961–99. *J. Hydrometeorol.* **10**, 60–78 (2009).
30. Ahlström, A. P. *et al.* Seasonal velocities of eight major marine-terminating outlet glaciers of the Greenland ice sheet from continuous *in situ* GPS instruments. *Earth Syst. Sci. Data* **5**, 277–287 (2013).
31. Joughin, I., Smith, B., Howat, I. & Scambos, T. *MEASURES Greenland Ice Velocity: Selected Glacier Site Velocity Maps from InSAR* (NASA National Snow and Ice Data Center, 2011); <http://dx.doi.org/10.5067/MEASURES/CRYOSPHERE/nsidc-0481.001>
32. Joughin, I. *et al.* Seasonal speedup along the western flank of the Greenland Ice Sheet. *Science* **320**, 781–783 (2008).
33. Palmer, S., Shepherd, A., Nienow, P. & Joughin, I. Seasonal speedup of the Greenland Ice Sheet linked to routing of surface water. *Earth Planet. Sci. Lett.* **302**, 423–428 (2011).
34. van de Wal, R. S. W. *et al.* Large and rapid melt-induced velocity changes in the ablation zone of the Greenland Ice Sheet. *Science* **321**, 111–113 (2008).
35. Tedstone, A. J. *et al.* Greenland ice sheet motion insensitive to exceptional meltwater forcing. *Proc. Natl Acad. Sci. USA* **110**, 19719–19724 (2013).
36. van de Wal, R. S. W. *et al.* Self-regulation of ice flow varies across the ablation area in south-west Greenland. *Cryosphere* **9**, 603–611 (2015).
37. Gudmundsson, G. H. *et al.* High-resolution measurements of spatial and temporal variations in surface velocities of Unteraargletscher, Bernese Alps, Switzerland. *Ann. Glaciol.* **31**, 63–68 (2000).
38. Burgess, E. W., Larsen, C. F. & Forster, R. R. Summer melt regulates winter glacier flow speeds throughout Alaska. *Geophys. Res. Lett.* **40**, 6160–6164 (2013).
39. Dow, C. F., Kulesa, B., Rutt, I. C., Doyle, S. H. & Hubbard, A. Upper bounds on subglacial channel development for interior regions of the Greenland ice sheet. *J. Glaciol.* **60**, 1044–1052 (2014).
40. Dow, C. F. *et al.* Modeling of subglacial hydrological development following rapid supraglacial lake drainage. *J. Geophys. Res.* 2014JF003333 (2015).
41. Doyle, S. H. *et al.* Persistent flow acceleration within the interior of the Greenland ice sheet. *Geophys. Res. Lett.* **41**, 899–905 (2014).
42. Bougamont, M. *et al.* Sensitive response of the Greenland Ice Sheet to surface melt drainage over a soft bed. *Nature Commun.* **5**, 5052 (2014).
43. Bintanja, R. & Selten, F. M. Future increases in Arctic precipitation linked to local evaporation and sea-ice retreat. *Nature* **509**, 479–482 (2014).
44. Fettweis, X., Belleflamme, A., Erpicum, M., Franco, B. & Nicolay, S. in *Climate Change: Geophysical Foundations and Ecological Effects* (eds Blanco, J. & Kheradmand, H.) 503–520 (InTech, 2011).
45. Franco, B., Fettweis, X. & Erpicum, M. Future projections of the Greenland Ice Sheet energy balance driving the surface melt. *Cryosphere* **7**, 1–18 (2013).
46. Box, J. E. *et al.* Greenland ice sheet albedo feedback: Thermodynamics and atmospheric drivers. *Cryosphere* **6**, 821–839 (2012).
47. IPCC *Climate Change 2013: The Physical Science Basis* (eds Stocker, T. F. *et al.*) (Cambridge Univ. Press, 2013).

Acknowledgements

This research was financially supported by: SKB/Posiva through the Greenland Analogue Project (GAP); UK National Environment Research Council (NERC) grants NE/G005796/1, NE/G010595/1, NE/H024204/1; a Royal Geographical Society Gilchrist Fieldwork Award; and The Netherlands Organisation for Scientific Research (NOW/PPP)—the last of which generously supported the K-transect measurements. TanDEM-X data were provided by the German Aerospace centre (DLR) within the framework of the XT1_GLAC0433 project. We thank UNAVCO, the National Snow and Ice Data Center, the Danish Meteorological Institute, MIT, J. Cappellen, R. Pettersson, K. Lindback and A. Fitzpatrick for help with data collection and processing. The crew of SV *Gambo* are thanked for help in the deployment of the Store Glacier GPS. A.H. and H.P. were supported at the Centre for Arctic Gas Hydrate, Environment and Climate by funding from the Research Council of Norway (Grant No. 223259). S.H.D. was supported by an Aberystwyth University doctoral scholarship and NERC grant NE/K006126.

Author contributions

A.H., S.H.D., T.W.M. and J.T.H. collected the dual-frequency GPS data. S.H.D. processed the dual-frequency GPS data, collated the data sets, prepared the figures and wrote the original manuscript. R.S.W.v.d.W. and P.C.J.P.S. provided the single-frequency GPS data, and together with F.W. acquired the borehole water pressure record. J.E.B. provided and interpreted the reanalysis data and advised on meteorology. D.v.A. collected and processed the AWS data sets and modelled the surface energy balance. K.S. processed the TanDEM-X data sets. E.J. applied the correction to the precipitation records. R.H.M. performed the HIRHAM5 regional climate modelling. B.H. advised on the analysis of borehole water pressure records and their relationship to ice velocity. H.P. processed the Terra SAR-X data for Jakobshavn Isbræ. P.C. and A.B.M. provided additional advice on data interpretation and analysis. All authors contributed to the subsequent editing of the manuscript. A.H. was the P.I. of the main project that conceived the study and co-developed it with S.H.D.

Additional information

Supplementary information is available in the [online version of the paper](#). Reprints and permissions information is available online at www.nature.com/reprints. Correspondence and requests for materials should be addressed to S.H.D.

Competing financial interests

The authors declare no competing financial interests.

Methods

GPS measurements of ice surface motion. We used five dual-frequency GPS receivers (R2, R13, I14, I27 and I46) capable of resolving three-dimensional ice surface velocities at a high temporal resolution (<1 h), and three single-frequency GPS receivers (R38, R52, and R88) capable of resolving horizontal ice surface velocities at a daily time step (Fig. 1).

Data from the dual-frequency receivers were processed kinematically⁴⁸ at a 30-s interval relative to bedrock-mounted reference stations using the carrier-phase differential-positioning software Track v. 1.24 (ref. 49) and final precise ephemeris from the International GNSS Service⁵⁰. Reference GPS stations were located 1 km from the terminus of Russell Glacier (BASE) and at Kellyville (KELY) giving baseline lengths of 5 to 46 km. Assuming steady ice motion, uncertainties in the positions were estimated at <0.02 m in the horizontal and <0.05 m in the vertical by examining the detrended position time series for GPS receiver R13 in early June 2011. High-frequency noise was filtered with a two-pole, low-pass Butterworth filter with a 12-h cutoff period. To reduce the effect of bed-parallel motion the surface height record presented in Fig. 3c was linearly detrended.

A sixth dual-frequency receiver was located at R140 (co-located with M140) but owing to the low velocity at this site ($\sim 52 \text{ m yr}^{-1}$), which is located 50 km above the long-term mean ELA, and the long baseline length (>140 km) a different, more rigorous, processing strategy was used to process data from this site and the methods are detailed in ref. 41.

The single-frequency receivers recorded horizontal position every hour and the resulting time series were filtered with a 48-h-period average⁵¹. We did not attempt to resolve vertical motion from the single-frequency GPS records as the detection limit is close to the magnitude of ice surface uplift⁵¹.

Daily averaged horizontal velocity was calculated by differencing the filtered positions at a daily time step. We calculated the annual velocity (Supplementary Table 1) from positions of the antenna on 6 June 2010 and 6 June 2011 for Russell Glacier GPS and from 2 September 2011 and 2 September 2012 for Isungata Sermia GPS. These dates were selected on the basis of available data and to avoid times when antenna poles were relocated (for example, 7 June 2011 for GPS R13 and R2).

To investigate whether ice-flow acceleration occurred in other regions of the GIS during the late-August/September 2011 event, we examined all available GPS records from published studies. Flow acceleration was evident in all available records with contemporaneous data, and these records are presented in Fig. 2d as daily averaged speed above the annual mean. These data from sites S11 and A20 are from Store Glacier and Sermeq Avannarleq and are adapted from refs 30 and 6 respectively. S11 consisted of an L1 GPS receiver located 11 km from the calving front of marine-terminating Store Glacier³⁰ and A20 consisted of a dual-frequency GPS receiver located at the FOXX borehole and AWS site⁶, ~ 20 km from the terminus of marine-terminating Sermeq Avannarleq (Supplementary Table 1), which is ~ 26 km down-glacier of Swiss Camp¹⁴. S11 flows an order of magnitude faster than all of the other GPS sites in Fig. 2d owing to its proximity to the calving front of this fast marine-terminating outlet glacier. The seasonal velocity cycle at S11 is also markedly different and can be explained by the influence of sea ice melange⁵². The magnitude and seasonal variation in velocity at A20 is, on the other hand, entirely consistent with the sites on Russell Glacier and Isungata Sermia (Fig. 2d).

TanDEM-X methods and verification against GPS records. We applied offset tracking on repeat-pass TanDEM-X data to derive surface velocities for the ice-sheet margin in August and September 2011. TanDEM-X (TerraSAR-X add-on for Digital Elevation Measurement) is a bistatic Synthetic Aperture Radar (SAR) mission launched in June 2010 with the two satellites orbiting in a closely controlled formation with typical distances between 250 and 500 m. The satellites circle on an 11-day repeat orbit, acquiring SAR images, with a 30×50 km footprint, at a 3 m spatial resolution⁵³.

We used three ascending images acquired on 1 August, 23 August, and 3 September 2011. We combined the first two acquisitions (1 August, 23 August; 22-day separation) to derive the 'average August' ice velocities, and the images recorded on 23 August and 3 September (11-day separation) for detecting the late-August acceleration (Supplementary Fig. 1). We computed SAR amplitude images for each of the scenes and applied an image-to-image cross-correlation technique to track the motion of features on the glacier surface⁵⁴.

The accuracy of the derived flow speeds was investigated by a comparison with velocities for the same time intervals at two GPS locations: R2 and R13 (see inset in Supplementary Fig. 1). We found good agreement for both periods, with differences ranging between 0.011 m d^{-1} (R2, 1–23 August) and 0.058 m d^{-1} (R13, 23 August–3 September).

In addition to the TanDEM-X measurements described above for the Kangerlussuaq sector, InSAR speed differences across the Jakobshavn Isbræ catchment were calculated from velocity maps derived from TerraSAR-X image pairs³¹ for a pre-event period (2–13 August 2011) and a period representing the event (23 August–3 September 2011; see Supplementary Fig. 3). Potential

control-related errors along the ice-sheet margin are presumed small ($<10 \text{ m a}^{-1}$) relative to variations in ice-flow speed, although height errors in the digital elevation model used for topographic correction in the original processing can yield absolute errors of up to $\sim 3\%$ of speed⁵⁵.

Borehole water pressure. We present data from a wired pressure sensor installed 0.5 m from the ice/bed interface at site R13/M13, and express borehole water pressure as a percentage of the ice overburden pressure assuming an ice thickness of 610 m and a density of ice of 917 kg m^{-3} (Fig. 3c). Further description of the methods used to drill and instrument the borehole is detailed in a previous study⁵⁶.

Meteorological measurements. Meteorological measurements were made by three on-ice AWS located 13 km (M13), 61 km (M61) and 140 km (M140) from the terminus of Russell Glacier, and one on-tundra AWS (M0) located 1 km west of the ice margin (Fig. 1 and Supplementary Table 2). To keep consistency with the GPS site names, the numbers in the AWS site labels refer to the distance from the terminus of Russell Glacier. The on-ice AWS were previously referred to as KAN_L (M13; co-located with R13), KAN_M (M61) and KAN_U (M140; co-located with R140), and we direct the reader to ref. 57 for further information on the AWS methods. The AWS recorded surface height change due to accumulation and ablation, air pressure, temperature and humidity, wind speed and direction, and downward and upward short-wave and long-wave radiation at 2–3 m above the surface. The AWS sampled at a 10-min interval, from which hourly averages were calculated. The energy available for melt was determined using a surface energy balance model⁵⁸, validated using the AWS measurements of surface temperature and surface height change⁵⁷.

Estimating cloud cover and the freezing level. Cloud cover was approximated making use of the strong dependence of downwards long-wave radiation on atmospheric moisture⁵⁸. A full cloud cover was assumed for high downward long-wave radiation values at a certain air temperature, and clear skies for low values, with a linear transition for values in between. We estimated the elevation of the freezing level using lapse rates calculated from M61 and M140 air temperature measurements.

Precipitation measurements. Precipitation records from site M0 and Kangerlussuaq (DMI station 04231; ref. 59) were corrected for wind and adhesion loss effects, using site-specific correction factors^{60,61}. We applied correction factors of 33% for snow and 16% for rain for the automatic GEONOR gauge deployed <1 km from the ice margin at M0, a site that is exposed to the wind. For the manual gauge at Kangerlussuaq, which is more sheltered from the wind, we applied correction factors of 12% for snow and 4.5% for rain. At both sites the adhesion loss was set to 0.1 mm per precipitation event, and mass loss due to evaporation was assumed to be zero.

Decomposing the surface energy budget. We gained further insight into the abnormal runoff caused by this weather event by decomposing the surface energy budget (SEB) for the AWS at site M13 (Fig. 3a) on Russell Glacier. The net short-wave (SW_{net}) and net long-wave (LW_{net}) radiation, the sensible (SHF) and latent (LHF) heat fluxes and the ground flux are defined as positive when they add heat to the surface.

Although clouds reduce net short-wave radiation, through the so-called long-wave cloud effect they can increase LW_{net} as a larger fraction of the outgoing long-wave radiation is absorbed by clouds and re-radiated back to the surface^{17,62}. LW_{net} typically represents a heat sink in the SEB but under certain atmospheric conditions^{16,63} it can be positive resulting in higher net radiation ($R_{\text{net}} = \text{SW}_{\text{net}} + \text{LW}_{\text{net}}$) than under clear skies. Accordingly, although daily total SW_{net} on 27 August was less than half ($4.9 \text{ MJ m}^{-2} \text{ d}^{-1}$) that recorded under clear-sky conditions seven days previously on 21 August ($10.3 \text{ MJ m}^{-2} \text{ d}^{-1}$), net radiation was greater on the 27 August ($5.2 \text{ MJ m}^{-2} \text{ d}^{-1}$) compared with 21 August ($4.5 \text{ MJ m}^{-2} \text{ d}^{-1}$) owing largely to the LW_{net} being positive (Fig. 3a). The largest energy source during the event was, however, the SHF, which accounted for more than 50% of the surface energy budget between 26 to 28 August—a marked increase on the pre-event values (for example, 19% on 21 August 2011) under clear skies (Supplementary Fig. 2a) and with low wind speeds (Supplementary Fig. 2b). The increase in SHF can be attributed to the high near-surface temperature resulting from the advection of warm air over the ice sheet (Fig. 4). Moisture condensation onto the ice surface due to high specific humidity and wind speed resulted in a positive LHF (for example, $3.0 \text{ MJ m}^{-2} \text{ d}^{-1}$, or 18% of the SEB on 27 August), as opposed to surface evaporative cooling (for example, $-0.73 \text{ MJ m}^{-2} \text{ d}^{-1}$ on 21 August), which is more frequent under the prevalent clear-sky conditions (Fig. 3a). Both turbulent heat fluxes (SHF and LHF) are enhanced by high wind speeds (for example, 8 m s^{-1} on 27 August; Supplementary Fig. 2b), which increase the vertical mixing of air^{17,64}.

For a given air temperature, moist conditions have lower lapse rates and therefore higher freezing levels than dry conditions. The lapse rate during the

late-August event (24–31 August) was much lower ($0.48\text{ }^{\circ}\text{C } 100\text{ m}^{-1}$) than the annual mean ($0.70\text{ }^{\circ}\text{C } 100\text{ m}^{-1}$), resulting in the $0\text{ }^{\circ}\text{C}$ isotherm attaining an exceptionally high elevation of $\sim 2,450\text{ m}$ asl on 27 August 2011. Air temperatures at M61 (1,280 m asl) were continuously above freezing during the late-August event (Fig. 2a). Even at M140, $\sim 50\text{ km}$ inland from the mean 1990–2011 ELA, positive air temperatures suggest that precipitation was liquid at least 140 km inland (Supplementary Fig. 2c).

The surface energy balance model does not account for the heat delivered by rain, which we found was minimal. The heat flux of rain Q_R is given by:

$$Q_R = \rho_w C_w R (T_r - T_s)$$

where ρ_w is the density of water, C_w is the specific heat capacity of water ($4.2\text{ kJ kg}^{-1}\text{ K}^{-1}$), R is the rainfall rate, and T_r and T_s are the temperatures of rain and the surface respectively⁶⁵. Given a surface temperature of a melting ice surface of $0\text{ }^{\circ}\text{C}$, a rain temperature of $6\text{ }^{\circ}\text{C}$, and the lower (15 mm) and upper (24 mm) estimates of rainfall during the event we estimate that the rain heat flux contributed $0.06\text{--}0.1\text{ MJ m}^{-2}\text{ d}^{-1}$. This is equivalent to $1.1\text{--}1.8\text{ mm}$ w.e. of rain-induced ice melt during the entire event, which represents a small component of the runoff during the event (for example, 0.5% at M13).

At higher elevations the sensible and latent heat released by rainfall cooling and freezing in a surface snowpack may, however, have played an important role in bringing the sub-freezing snowpack to the melting point. The energy flux Q_R supplied by rain freezing in a snowpack is given by:

$$Q_R = \rho_w C_s R (T_r - T_s) + \rho_w \lambda_w R$$

where C_s is the specific heat capacity of snow ($2,090\text{ J kg}^{-1}\text{ K}^{-1}$), and λ_w is the latent heat of fusion (334 kJ kg^{-1}). The rain temperature of $2\text{ }^{\circ}\text{C}$ is taken to be the air temperature at M140 during the rainfall event and the temperature of the snowpack of $-15\text{ }^{\circ}\text{C}$ is based on the mean air temperature during the preceding week. Given these estimates, 14 mm of rain at $2\text{ }^{\circ}\text{C}$ would bring a 15 cm w.e. snowpack at $-15\text{ }^{\circ}\text{C}$ to the melting point. Hence, the energy released by rain cooling and freezing is a very effective heating mechanism for sub-freezing snowpacks and this will have enhanced melt rates at high elevations.

All of these energy sources—an abnormally positive net long-wave radiation, the sensible heat flux, the latent heat flux from condensation and the rain heat flux—contributed to high melt conditions peaking on 27 August, coincident (Fig. 2b) with the highest precipitation (Fig. 2a,b), wind speeds (Supplementary Fig. 2b), and freezing level (Supplementary Fig. 2c), which combined to produce abnormally high-magnitude runoff for this time of year (Fig. 2).

Calculating the elevation of the snowline. The elevation of the snowline—the maximum elevation that snow remains at the end of the melt season—was retrieved from end-of-melt-season visible-band Moderate Resolution Imaging Spectrometer (MODIS) images. The ice-sheet-wide, MODIS-retrieved snowlines, which are calibrated against the K-transect surface mass balance observations¹⁸, are available at <https://sites.google.com/site/jboxgreenland/greenland-ice-sheet-snowline>.

Reanalysis. We used data from the National Centers for Environmental Prediction/National Centre for Atmospheric Research (NCEP/NCAR) reanalysis project²⁷ to track weather systems, and to estimate precipitation and the near-surface air temperature anomaly over Greenland (Fig. 4 and Supplementary Figs 4–6 and 9–12). These reanalysis data reveal that a low-pressure system (minimum surface pressure of 992 hPa) tracking across Baffin Bay between 24 and 30 August 2011 caused warm southwesterly airflow (Fig. 4), which resulted in cloud cover (Supplementary Fig. 2a) and precipitation (Fig. 4) over southern and western Greenland. Such Baffin Bay cyclones represent the most common synoptic pattern to bring precipitation to Greenland²⁹. They often bifurcate over the southern GIS forming an Icelandic Low by lee cyclogenesis on the southeast coast, while the parent cyclone tracks north delivering precipitation to the west coast of Greenland^{28,29}. They advect warm moist air onshore from the open North Atlantic, which is lifted orographically over the ice sheet to an elevation of 2,800 m asl in less than 200 km (ref. 29). As the air rises, it cools adiabatically becoming saturated and releasing precipitation. Baffin Bay cyclones occur more frequently during the summer (6.35% of days) than during winter (2.90% of days)²⁹ and atmospheric models⁴ predict that they will increase in frequency from 3% of days in 1961–1999 to 4% of days in 2081–2100. The widespread nature of the precipitation and heat delivered by the August–September 2011 event is demonstrated by the reanalysis data (Fig. 4 and Supplementary Fig. 9) and acceleration in ice flow is evident in all available velocity records from southern and western Greenland during this period (Figs 1 and 2d and Supplementary Fig. 3). Substantial acceleration was measured on three major marine-terminating glaciers in West Greenland, including Sermeq Avannarleq⁶, Store Glacier³⁰ and Jakobshavn Isbræ (Fig. 2d and Supplementary Fig. 3).

Investigating long-term trends in rainfall seasonality. To investigate changes in the seasonal distribution of rainfall over the past two to three decades we examined long-term trends in the Kangerlussuaq precipitation record⁵⁹ between 1977 and 2012. The phase of precipitation was determined as liquid if the mean temperature over the corresponding 12-h period was greater than or equal to $2\text{ }^{\circ}\text{C}$, allowing daily total rainfall to be calculated.

Following standard statistical measures applied by previous studies^{66,67} we calculated the seasonality index (SI) and the day of year on which the 10th (P10), 25th (P25), 50th (P50), 75th (P75) and 90th (P90) percentiles of the annual total rainfall were achieved. We assessed the dispersion in the seasonal distribution of rainfall by calculating the interquartile (IQR = P75 – P25) and interdecile range (IDR = P90 – P10). The SI:

$$SI = \frac{1}{R} \sum_{n=1}^{12} \left| \bar{X}_n - \frac{R}{12} \right|$$

where R is the total annual rainfall and \bar{X}_n is the total monthly rainfall in month n , is a standard measure of rainfall seasonality⁶⁷. SI theoretically ranges from 0, if all of the months have equal rainfall to 1.83, if all of the rainfall falls in one month. SI values of 1–1.19 indicate that most rainfall occurs in 3 months or less with $SI > 1.2$ indicating that most rainfall falls in 2 months or less.

We investigated the timing of heavy rainfall events by calculating the fortnightly totals of rainfall for the entire Kangerlussuaq precipitation record. To normalize the influence of exceptional events between years, we divided fortnightly precipitation sums by their respective annual total (Fig. 5a). Heavy rainfall events, identified as dark red blocks on Fig. 5a, tend to occur more frequently in late summer and early autumn, coinciding with the period of highest rainfall¹⁵, peak long-wave radiation, densest cloud cover¹⁷ and peak cyclonic activity²⁵ in this region.

HIRHAM5 methods. We examined changes in rainfall across the K-transect¹⁸ over the past two decades using the HIRHAM5 regional climate model⁶⁸ (RCM). The HIRHAM5 RCM is driven at the lateral boundaries by the ERA-Interim reanalysis⁶⁹ and provides estimates of solid and liquid precipitation at 5 km horizontal resolution. The simulations are validated against observations from meteorological stations on the land⁵⁹ and AWS on the ice sheet^{57,70}. Generally, the temperature and precipitation biases are small, indicating a realistic simulation of the climate over Greenland⁷¹. We averaged the rain fraction estimated by the HIRHAM5 RCM over two periods (1990–1999 and 2000–2009) at each grid cell along the K-transect at a weekly time step (Fig. 5c).

References

- King, M. Rigorous GPS data-processing strategies for glaciological applications. *J. Glaciol.* **50**, 601–607 (2004).
- Chen, G. *GPS Kinematic Positioning for the Airborne Laser Altimetry at Long Valley, California* (Massachusetts Institute of Technology, 1998).
- Dow, J. M., Neilan, R. E. & Rizos, C. The International GNSS Service in a changing landscape of Global Navigation Satellite Systems. *J. Geod.* **83**, 191–198 (2009).
- Den Ouden, M. A. G. *et al.* Stand-alone single-frequency GPS ice velocity observations on Nordenskiöldbreen, Svalbard. *Cryosphere* **4**, 593–604 (2010).
- Walter, J. I. *et al.* Oceanic mechanical forcing of a marine-terminating Greenland glacier. *Ann. Glaciol.* **53**, 181–192 (2012).
- Krieger, G. *et al.* TanDEM-X: A satellite formation for high-resolution SAR interferometry. *IEEE Trans. Geosci. Remote Sensing* **45**, 3317–3341 (2007).
- Strozzi, T., Luckman, A., Murray, T., Wegmuller, U. & Werner, C. L. Glacier motion estimation using SAR offset-tracking procedures. *IEEE Trans. Geosci. Remote Sensing* **40**, 2384–2391 (2002).
- Joughin, I., Smith, B. E., Howat, I. M., Scambos, T. & Moon, T. Greenland flow variability from ice-sheet-wide velocity mapping. *J. Glaciol.* **56**, 415–430 (2010).
- Smeets, C. J. P. *et al.* Instruments and methods—A wireless subglacial probe for deep ice applications. *J. Glaciol.* **58**, 841–848 (2012).
- van As, D. *et al.* Large surface meltwater discharge from the Kangerlussuaq sector of the Greenland ice sheet during the record-warm year 2010 explained by detailed energy balance observations. *Cryosphere* **6**, 199–209 (2012).
- van As, D. Warming, glacier melt and surface energy budget from weather station observations in the Melville Bay region of northwest Greenland. *J. Glaciol.* **57**, 208–220 (2011).
- Cappelen, J. *et al.* *Weather Observations from Greenland 1958–2012* Technical Report 13-11 (Danish Meteorological Institute, 2013); <http://www.dmi.dk/fileadmin/Rapporter/TR/tr13-11.pdf>
- Alexandersson, H. *Korrektion av Nederbord Enligt Enkel Klimatologisk Metodik* (Meteorologi Nr 111, SMHI, 2003).
- Johansson, E. *et al.* Hydrological and meteorological investigations in a periglacial lake catchment near Kangerlussuaq, west Greenland—presentation of a new multi-parameter dataset. *Earth Syst. Sci. Data* **7**, 93–108 (2015).

62. Ambach, W. The influence of cloudiness on the net radiation balance of a snow surface with high albedo. *J. Glaciol.* **13**, 73–84 (1974).
63. Bennartz, R. *et al.* July 2012 Greenland melt extent enhanced by low-level liquid clouds. *Nature* **496**, 83–86 (2013).
64. van den Broeke, M. *et al.* Partitioning of melt energy and meltwater fluxes in the ablation zone of the west Greenland ice sheet. *Cryosphere* **2**, 179–189 (2008).
65. Hock, R. Glacier melt: A review of processes and their modelling. *Prog. Phys. Geogr.* **29**, 362–391 (2005).
66. Pryor, S. C. & Schoof, J. T. Changes in the seasonality of precipitation over the contiguous USA. *J. Geophys. Res.* **113**, D21108 (2008).
67. Walsh, R. P. D. & Lawler, D. M. Rainfall seasonality: Description, spatial patterns and change through time. *Weather* **36**, 201–208 (1981).
68. Christensen, O. B. *et al.* *The HIRHAM Regional Climate Model Version 5* Technical Report 06-17 (Danish Meteorological Institute, 2006); <http://www.dmi.dk/fileadmin/Rapporter/TR/tr06-17.pdf>
69. Dee, D. P. *et al.* The ERA-Interim reanalysis: Configuration and performance of the data assimilation system. *Q. J. R. Meteorol. Soc.* **137**, 553–597 (2011).
70. van de Wal, R. S. W., Greuell, W., van den Broeke, M. R., Reijmer, C. H. & Oerlemans, J. Surface mass-balance observations and automatic weather station data along a transect near Kangerlussuaq, West Greenland. *Ann. Glaciol.* **42**, 311–316 (2005).
71. Lucas-Picher, P. *et al.* Very high resolution regional climate model simulations over Greenland: Identifying added value. *J. Geophys. Res.* **117**, D02108 (2012).